Thermal Science and Engineering Progress 68 (2025) 104328

Contents lists available at ScienceDirect

Thermal Science and Engineering Progress

journal homepage: www.sciencedirect.com/journal/thermal-science-and-engineering-progress

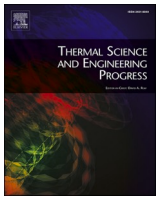

Acceleration effect on operating behavior of a visual loop heat pipe without a bayonet

Yongqi Xie [a], Lijun Chen [a], Jiayi Bao [a,*], Huifeng Kang [b], Zhen Fang [a], Hongwei Wu [c,*]

[a] School of Aeronautic Science and Engineering, Beihang University, Beijing 100191, China
[b] School of Aerospace Engineering, North China Institute of Aerospace Engineering, Langfang 065000, China
[c] School of Physics, Engineering and Computer Science, University of Hertfordshire, Hatfield AL10 9AB, UK

ARTICLE INFO

Keywords:
Thermal management
Loop heat pipe
Elevated acceleration
Visualization
Operational performance

ABSTRACT

This study proposes a newly designed ammonia-stainless steel dual compensation chamber loop heat pipe without a bayonet and experimentally investigates its operating performance under high acceleration (3–15 g) across four typical directions (A, B, C, and D), thermal loads (30–400 W), and heat sink temperatures (10–25 °C), using visual windows at the ends of the two compensation chambers to observe the internal vapor–liquid phase distribution. Experimental results indicate that (i) higher thermal loads increase operational temperature while thermal conductance initially increases and then stabilizing or decreasing, with stable operation achieved even under the most adverse direction A of 30 W and 9 g; (ii) directional effects are significant, with operational temperature decreases and thermal conductance increases sequentially from directions A to D. Direction D yields the lowest operational temperature of 27.8 °C at 3 g and 150 W, and highest thermal conductance of 23.12 W/K at 12 g and 200 W; (iii) vapor backflow may occur in the liquid pipe before startup in direction C, while high thermal loads operating during steady state could induce two-phase states in both condenser and liquid pipe; (iv) increased acceleration degrades operational performance in direction A, but slightly increases temperature in directions C and D, with thermal conductance varying by thermal load; and (v) higher heat sink temperature elevates operational temperature and thermal conductance while altering two-phase distribution in both the liquid pipe and condenser.

1. Introduction

The performance of modern advanced aircraft continues to improve, driven by the increasing miniaturization and integration of onboard electronic devices. These devices generate high heat flux, with localized values in some chips exceeding 500 W/cm^2 [1]. Traditional air and single-phase liquid cooling technologies are insufficient to meet the stringent thermal management requirements [2,3]. Consequently, the development of efficient two-phase cooling technology has become essential [4–7]. The loop heat pipe (LHP) offers a promising phase-change heat transfer solution, with advantages such as long-distance heat transfer, high heat transport capacity, superior thermal efficiency, energy savings, and ease of installation [8–11]. These features position LHPs as a transformative solution for managing onboard electronic device thermal challenges [12,13].

However, single CC LHPs may perform worse or even fail to operate due to unfavorable orientation preventing the working fluid to return to the CCs in terrestrial gravity [14], especially in varying and elevated acceleration environments [15]. Therefore, dual CC LHPs (DCCLHPs) were developed to address liquid supply issues caused by adverse orientations [16,17], making them suitable for onboard electronics cooling. Literature review indicates that almost all current studies employ bayonet structures. It has been demonstrated that bayonet structure has some advantages, particularly in microgravity environments where it can facilitate liquid working fluid flow to ensure sufficient wetting of the primary wick. Additionally, research has revealed that under high heat leak conditions, the bayonet could decrease the capillary force [18]. Furthermore, with large working fluid charge, the bayonet structure could lead to CC overheating and even the system failure [19].

Lin et al. [20] developed a bayonet-equipped DCCLHP, demonstrating its adaptability to different orientations and improved startup performance. Further studies [21] on ammonia-charged DCCLHPs analyzed orientations and thermal load effects on startup

* Corresponding authors.
E-mail addresses: xyq@buaa.edu.cn (Y. Xie), cljzy2305514@buaa.edu.cn (L. Chen), 11183@buaa.edu.cn (J. Bao), huifengabc596@163.com (H. Kang), h.wu6@herts.ac.uk (H. Wu).

https://doi.org/10.1016/j.tsep.2025.104328
Received 23 April 2025; Received in revised form 19 July 2025; Accepted 13 November 2025
Available online 14 November 2025

Nomenclature

Symbols

a	Acceleration, [m/s^2]
g	Gravitational acceleration, [9.81 m/s^2]
G	Thermal conductance, [W/K]
h	Latent heat of vaporization, [J/kg]
I	Current, [A]
L	Length, [m]
p	Pressure, [Pa]
Q	Thermal load, [W]
T	Temperature, [℃]
U	Uncertainty
V	Voltage, [V]
v	Specific volume of working fluid, [m^3/kg]
x	Independent variable
Y	Physical quantity

Greek symbols

ρ	Density, [kg/m^3]

Subscripts

a	Acceleration
c	Condenser
e	Evaporator
in	Inlet
lp	Liquid pipe
out	Outlet
sat	Saturation
tot	Total pressure drop
vg	Vapor groove
vl	The difference in specific volume between the saturated vapor and saturated liquid
vp	Vapor pipe
w	Wick
wcp	Water-cooling plate

Acronyms

CC	Compensation chamber
DCCLHP	Dual compensation chamber loop heat pipe
EPDM	Ethylene propylene diene monomer
ID	Inside diameter
LHP	Loop heat pipe
OD	Outside diameter

characteristics, revealing operational instabilities such as reverse flow, temperature hysteresis, and temperature oscillations, with oscillations occurring more frequently when the bayonet-equipped CC was above the evaporator [22]. Su et al. [23] investigated the operating performance of a DCCLHP with a bayonet using an ethanol–water mixture as the working fluid at three different tilt angles. It was found that a 60 % concentration mixture enabled the DCCLHP to achieve lower operational temperature and thermal resistance at 300 W, while reducing the startup time by 30.18 % compared to pure ethanol conditions. Bai et al. [24,25] proposed two ammonia-charged DCCLHPs with extended and dual bayonets to enhance startup performance at various orientations. Experimental results showed that successful startup at low thermal loads (10 W) across all tested orientations, though temperature overshoot was observed due to liquid accumulation in vapor grooves [24]. Under anti-gravity conditions with increased operational temperature, the DCCLHP achieved effective heat transport of approximately 430 W over a 2.0 m distance, attaining a minimum thermal resistance of 0.067 K/W [25]. Yang et al. [26] examined an ammonia-charged DCCLHP with the bayonet and an eccentric ceramic wick, demonstrating startup at 2 W and a heat transport capacity exceeding 450 W over 2.0 m, with a small CC temperature differential enhancing performance. Fu et al. [27,28] designed and investigated the operating performance of two ammonia-charged DCCLHPs featuring the bayonet, with dual vapor and condenser lines, and a CC cooling structure respectively. Their results showed that temperature overshoot and oscillations primarily occurred at low thermal loads. The DCCLHP achieved a heat transfer capacity of over 600 W at a 1.1 m distance, and the adoption of dual vapor and condenser lines significantly reduced flow resistance [27]. Additionally, sequential CC cooling improved startup performance, reduced startup time, and lowered thermal resistance [28]. Wang et al. [29,30] investigated an ammonia-stainless steel DCCLHP capable of 1 kW heat transfer, revealing the effects of orientation and elevated acceleration on its performance. It was found that mechanical forces may alter the thickness of the condensate film in the condenser, thereby influencing the overall performance of the DCCLHP. Furthermore, Xie et al. [31,32] systematically investigated nickel-ammonia DCCLHP performance under various acceleration directions and magnitudes, thermal loads, and loading modes, providing insights into acceleration-induced phenomena.

Visualization techniques serve as an effective methodological approach for directly capturing the vapor–liquid phase distribution and flow patterns within the LHP, thereby enhancing the fundamental understanding of its heat and mass transfer mechanisms. In recent years, a growing number of researchers have employed visualization methods to investigate operating performance of the LHPs [33–36]. Cimbala and Okamoto et al. [37–39] pioneered neutron radiography to visualize two-phase flow and wick dry-out in the LHP with a bayonet, using ammonia and water as working fluids, respectively. Lin et al. [40] used transparent glass windows to investigate the effects of thermal load, initial vapor–liquid phase distribution, and orientation on both startup and operating performance of an ammonia-charged DCCLHP with the bayonet. Their work revealed that radial heat leakage in the evaporator was the fundamental cause of various phenomena including bubble formation, liquid redistribution, fluctuated flow and reverse flow within the evaporator core. Zhao et al. [41] experimentally investigated the operating performance of a DCCLHP with a bayonet using ethanol as the working fluid, with particular focus on angle of attack effects. It was demonstrated that the angle of attack significantly affected evaporator and condenser temperatures, inducing oscillations. Nishikawara et al. [42–44] employed a transparent tube as the evaporator shell to observe and analyze the transient behavior on the wick's exterior surface in a LHP without a bayonet, using acetone as the working fluid. It was illustrated that under eight initial vapor–liquid phase distributions, meniscus oscillations at the three-phase contact line were observed in nearly all cases, accompanied by boiling in the CC. Moreover, the meniscus receded with increasing heat flux, influencing the evaporator heat transfer coefficient. Chang et al. [45–47] visually investigated a bayonet-equipped LHP with dual evaporators and a condenser using acetone as the working fluid. Results showed that the two-phase flow region was longer and heat leakage lower in gravity-driven mode than in capillary-gravity mode. More pronounced condenser oscillations were observed in both anti-gravity and gravity-assisted conditions compared to horizontal operation. Zhang et al. [48] experimentally investigated the operating performance of a semi-cylindrical glass-sealed LHP with a bayonet, using acetone as the working fluid, under varying thermal loads and angles. It was found that multiple bubble motion patterns existed in the core, and the oscillation of the vapor–liquid phase interface within the evaporator core was the direct cause of the temperature

fluctuation. Liu et al. [49] proposed a novel LHP with a vapor-driven jet injector and investigated its temperature oscillation mechanisms using deionized water. It was found that high-amplitude temperature oscillations resulted from intermittent liquid supply in the CC. Increasing the heat sink temperature or reducing the filling ratio could eliminate these oscillations. Yan et al. [50] investigated the two-phase behavior in the condenser of a LHP using propylene as the working fluid. It was demonstrated that the reduction of two-phase zone length and increased condenser outlet subcooling led to enhanced heat leakage from the evaporator to the CC. Xie et al. [51,52] conducted a visual investigation on the operational performance of a water-stainless steel DCCLHP with a bayonet in acceleration environment. It was revealed that intermittent droplet splashing occurred in the CCs at direction A. The alternating distribution of vapor and liquid columns in the condenser was found to significantly influence the total system pressure drop. Additionally, the stratified or annular flow pattern in the condenser was observed to affect thin-film condensation heat transfer. Through visualization techniques and numerical simulations, Zhou et al. [53] studied the effects of vapor groove dimensions on both thermal efficiency and vapor–liquid phase distribution in a LHP with a bayonet using R245fa as the working fluid. Their results demonstrated a strong correlation between the evaporator heat transfer coefficient and the liquid film thickness within the vapor grooves.

In summary, current research has primarily focused on the operational performance of the LHP with bayonet structures, validating their beneficial role in low-power startup. For the DCCLHP, existing studies have confirmed reliable operation under all orientations. Removing the bayonet reduces weight and simplifies manufacturing processes. Furthermore, compared to working fluids such as deionized water, acetone, ethanol and propylene, ammonia exhibits superior

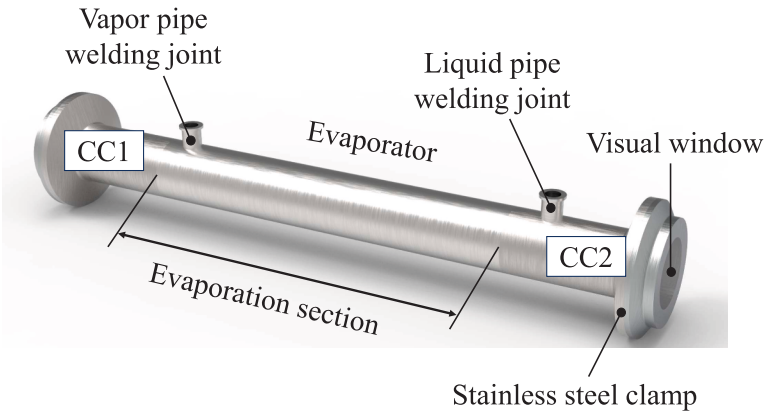

(a) The schematic diagram of the external structure of the evaporator and CCs

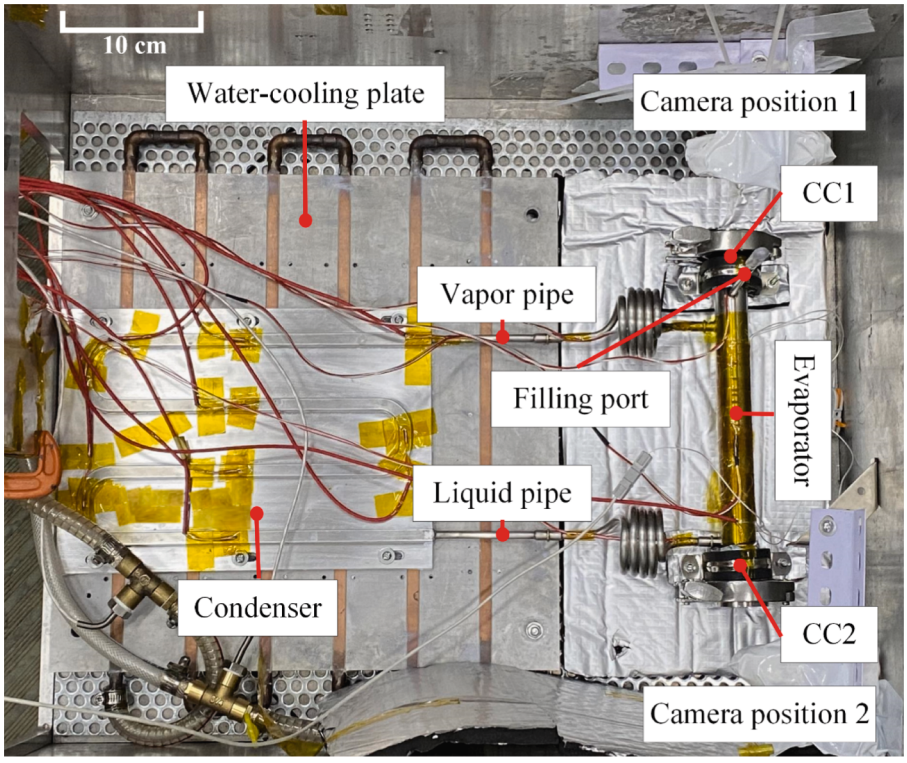

(b) The photo of the visual DCCLHP testing unit

Fig. 1. The schematic diagram of the evaporator and CCs and photo of the visual DCCLHP.

comprehensive properties including higher latent heat, lower surface tension and greater dp/dT slope [54], enabling excellent thermal performance in the LHP. However, the ammonia-charged LHP exhibits significantly higher system pressure compared to those using alternative working fluids, and ammonia manifests incompatibility with common sealing materials. These pose substantial challenges for implementing transparent glass visualization, particularly in high acceleration environment. Moreover, no relevant studies have been reported.

Despite various visualization studies on LHPs, current understanding of two-phase flow dynamics and heat transfer phenomena remains incomplete. To the best of the authors' knowledge, investigations of dynamic operational behaviors, internal flow dynamics, and heat transfer mechanisms in DCCLHP systems, particularly subjected to elevated acceleration conditions, are still quite limited. Therefore, the current study pioneers a visualization-based approach to elucidate the internal vapor–liquid distribution and flow patterns of a DCCLHP without a bayonet under elevated acceleration fields while identifying novel thermofluidic phenomena. The impacts of several key parameters, including varying acceleration directions, magnitudes, thermal loads, and heat sink temperatures, will be systematically examined in both transient and steady-state conditions. Findings will advance DCCLHP applications in next-generation aircraft thermal management, providing both theoretical insights and practical guidance.

2. Experimental descriptions

2.1. Specifications of visual DCCLHP

In the present work, a newly designed and visual ammonia-stainless steel DCCLHP without the bayonet structure was fabricated by Shanghai Geentropy Aerospace Technology Co., Ltd. to observe the flow pattern variations and vapor–liquid phase distribution inside the CCs, as illustrated in Fig. 1. The key design parameters of the visual DCCLHP are summarized in Table 1.

Fig. 1(a) shows the schematic diagram of the external structure of the evaporator and CCs. Notably, the liquid pipe is directly connected to the outer wall of CC2 without extending into the evaporator core, indicating the absence of a bayonet. The CCs are positioned at both ends of the evaporator and are connected via the evaporator core, ensuring the capillary wick liquid supply at all orientations, particularly under high acceleration effect. The sintered nickel capillary wick was fabricated using the powder metallurgy method, with an average pore diameter of 0.5 μm.

Fig. 1(b) presents the visual DCCLHP photo including the evaporator, two CCs with visual windows, a condenser, and vapor and liquid pipes. Both the vapor and liquid pipes incorporate helical configurations. The transparent windows are made of silicate tempered glass. To prevent work fluid leakage, ethylene propylene diene monomer (EPDM) sealing gaskets are employed on the interface of the CC shells and stainless-steel clamps. For ensuring a lightweight and corrosion-resistant design, the condenser tubing is made of stainless steel, exhibiting a 6 mm outer diameter with 5 mm inner diameter. The tubing is brazed to a lightweight aluminum plate measuring 280 mm × 200 mm.

Ammonia, due to its high saturation pressure gradient and low boiling superheat at ambient temperatures, generates sufficient driving force to overcome flow resistance even under small temperature difference. Additionally, its relatively low dynamic viscosity and surface tension help promote bubble nucleation and detachment [54]. Despite these advantages, visual studies of DCCLHP using ammonia as the working fluid are limited, particularly in high acceleration environment, with no reported investigations in this context. For these reasons, ammonia has been chosen as the working fluid in the current study.

Table 1
Principal design parameters of the DCCLHP.

Components	Material	Design parameters	Dimensions
Wick	Nickel	OD/ID/Length (mm)	23/10/156
		Pore radius (μm)	0.5
		Permeability (m^2)	1.3×10^{-14}
		Porosity	48.5 %
Evaporator	Stainless steel 316 L	OD/ID/Length (mm)	25/23/156
CCs	Stainless steel 316 L	OD/ID/Length (mm)	27/25/60
Vapor pipe	Stainless steel 316 L	OD/ID/Length (mm)	6/4/500
Liquid pipe	Stainless steel 316 L	OD/ID/Length (mm)	6/4/500
Condenser	Stainless steel 316 L	OD/ID/Length (mm)	6/5/1100
Working fluid	Ammonia		

2.2. Experimental setup

The schematic diagram of the testing rig is illustrated in Fig. 2. It mainly consists of four main subsystems: the acceleration control system, the data acquisition and heating control system, the recirculating water chiller system, and the visual DCCLHP testing unit.

The acceleration control system consists of a Y53100-3/ZF centrifugal acceleration regulating machine, a transducer controller, and a PC controller, which together create the required acceleration environment. At the extremity of the spiral arm, the centrifuge regulating machine has capable of generating radial accelerations up to 15 g. The data acquisition and heating control system includes PT100 temperature sensors, an Agilent 34970A data acquisition instrument, junction boxes, a remote PC, and a DC power supply. This system is connected to thin-film electric heaters, providing the necessary heat source for the evaporator. Temperatures at all measurement points on the DCCLHP are remotely monitored and automatically logged. The recirculating water chiller system comprises a cold-water chiller (Sanffo HK-30/20 L), a frequency converter, a pump, control valves, a filter, a Coriolis flowmeter (DMF1-2), a DC power supply, and an aluminum water-cooling plate. This system ensures a controllable and stable heat sink temperature for the visual DCCLHP.

The visual DCCLHP testing unit is securely mounted at the outer edge of the spiral arm of the centrifuge within a stainless-steel cabinet. It sustained a non-uniform acceleration force due to different distances from the DCCLHP to the centrifugal axis. The acceleration range of from 90 % to 130 % of the acceleration of the center over the testing unit should be achieved according to GB/T 2423.15. This setup includes the visual DCCLHP, two video cameras (GoPro HERO9), and two LED lights. The video cameras are configured to capture up to 60 fps with a frame resolution of 1520 × 2704 pixels, allowing for detailed observation of the vapor–liquid phase distribution in the two CCs. The two LED lights provide additional illumination for the cameras. The condenser is mounted on the water-cooling plate, with thermal grease applied to reduce contact resistance. To minimize heat leakage, the entire loop is wrapped with aluminum foil thermal insulation.

2.3. Experimental conditions

In this study, the impacts of various thermal loads, directions and magnitudes of acceleration, and heat sink temperatures on the operating performance of the developed DCCLHP were systematically studied by experiment. All experimental conditions are summarized in Table 2. For system reliability, six radial acceleration magnitudes were selected: 0 g, 3 g, 6 g, 9 g, 12 g and 15 g (with 0 g representing the terrestrial gravity environment). These magnitudes did not exceed the maximum allowable acceleration of the centrifuge. As illustrated in Fig. 3, four acceleration directions were specified, labeled as A, B, C, and D. The evaporator, CCs, and condenser of the visual DCCLHP testing unit were positioned horizontally, with gravity acting vertically downward. The acceleration direction A was aligned with the axis of the vapor and liquid pipes, which pointed toward the condenser located at the outer edge of the spiral arm, and was the opposite of direction C. For comparison, the acceleration directions of B and D were aligned with the axis of the evaporator. Direction B pointed toward CC2, whereas direction D

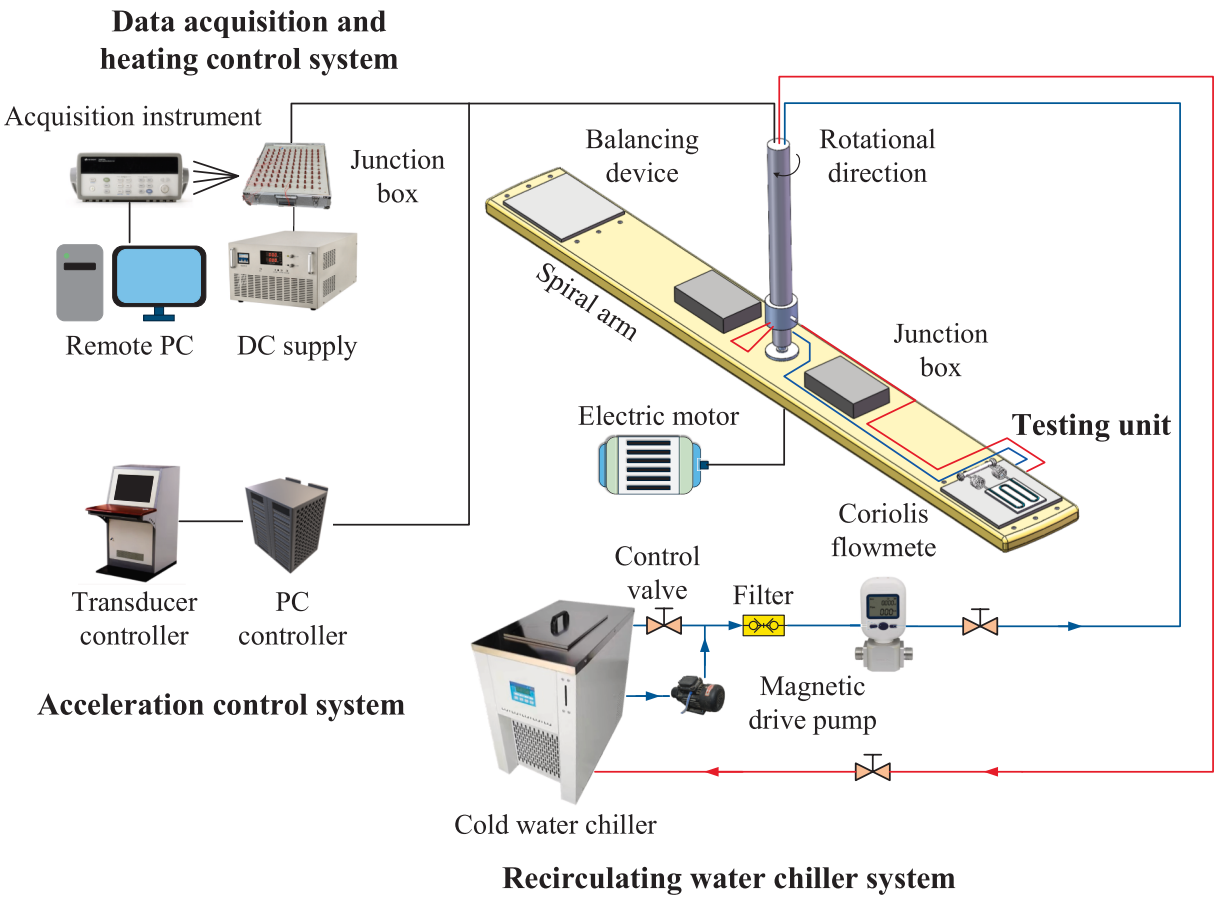

Fig. 2. Schematic diagram of visual DCCLHP testing rig.

Table 2
Selection of experimental conditions.

Parameter	Variation
Acceleration magnitude	0 g, 3 g, 6 g, 9 g, 12 g, 15 g
Acceleration direction	A, B, C, D
Thermal load (W)	30, 50, 100, 150, 200, 250, 300, 350, 400
Heat sink temperature (℃)	10, 15, 20, 25

pointed toward CC1. By rotating the entire cabinet by 90° using the spiral arm as a reference, the above four different acceleration directions could be exerted to the testing unit, as shown in Fig. 3.

For safety, the sustained operation of the centrifuge exhibited a strict one-hour duration threshold. The experiment achieved concurrent application of thermal load and centrifugal acceleration. The thermal load was adjusted based on the test requirements, with values set at 30 W, 50 W, 100 W, 150 W, 200 W, 250 W, 300 W, 350 W, and 400 W. However, not all thermal loads were tested across all acceleration directions. The environment temperature was maintained at approximately 25 ℃. The water-cooling plate temperature was controlled by adjusting the water temperature of the chiller, with inlet values set at 10 ℃, 15 ℃, 20 ℃, and 25 ℃.

A total of fifteen temperature measurement points were strategically placed along the entire loop, with their locations shown in Fig. 3. EVA is positioned at the midpoint of the evaporator external surface and represents the operational temperature of the DCCLHP. CC1 and CC2 are used to monitor temperature variations within the CCs. COLD_IN and COLD_OUT indicate the inlet and outlet temperatures of the water-cooling plate. VP_IN and VP_OUT are located at the front and rear of the vapor pipe, with VP_IN situated approximately 2.5 cm from the welding joint between the vapor pipe and the evaporator. Similarly,

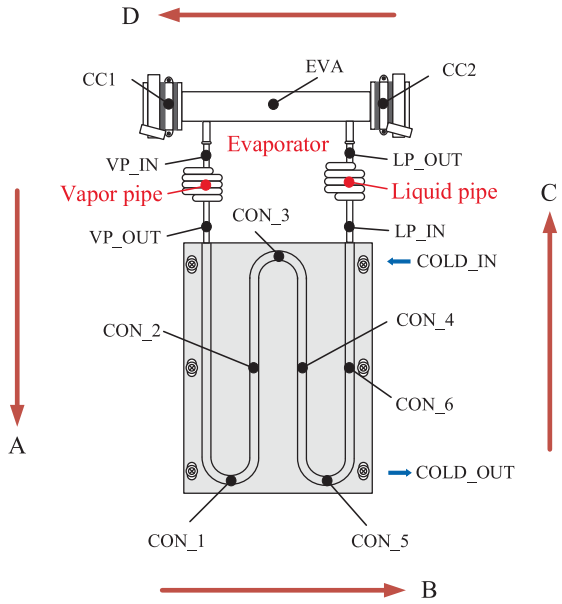

Fig. 3. The acceleration directions and location of temperature measurement points.

LP_IN and LP_OUT are located at the front and rear of the liquid pipe, with LP_OUT positioned approximately 2.5 cm from the welding joint between the liquid pipe and the CC2. Finally, CON_1 through CON_6 are arranged along the condenser tubing to monitor temperature distribution, with CON_1, CON_3 and CON_5 located at the bends of the

condenser tubing.

Calibration was performed for all the instruments before formal experiments. For PT100 temperature sensors calibration, a standard PT100 temperature sensor and thermostatic water bath were used. Two distinct temperature zones were divided based on the operating temperature. One was the temperature zone of the ambient temperature and the inlet and outlet water temperature of the water-cooling plate, in which there were 13-point calibration at 2 °C intervals from 8 °C to 32 °C. The other was the temperature zone of the loop temperature, in which the thirteen PT100 temperature sensors located on the DCCLHP were calibrated over the whole range of 10–50 °C in 2 °C increments.

2.4. Uncertainty analysis

If a physical quantity Y is a function of several independent variables x_1, x_2, …, x_n, its uncertainty can be formulated as follows [55]:

$$\frac{U(Y)}{Y} = \left[\sum_{i=1}^{n}\left(\frac{\partial Y}{\partial x_i}\delta x_i * \frac{1}{Y}\right)^2\right]^{1/2} \tag{1}$$

where δx_i is the uncertainty of the ith recorded variable.

In the current study, thermal conductance G, an important indicator of the DCCLHP's operating performance, is analytically described using the following equation [20]:

$$G = \frac{Q_e}{T_e - T_{wcp}} \tag{2}$$

where Q_e is the thermal load applied on the evaporator, T_e is the evaporator temperature. T_{wcp} is the average temperature of the water-cooling plate, it is determined by the following formula [40]:

$$T_{wcp} = \frac{T_{in} + T_{out}}{2} \tag{3}$$

where T_{in} and T_{out} are the inlet and outlet temperatures of the cooling water, respectively.

During the test, the primary source of uncertainty was the data acquisition system. The PT100 sensors exhibited a temperature measurement uncertainty of ± 0.3 ℃. The overall temperature uncertainty reached 4 % due to factors such as the electric wires, temperature sensors, electromechanical slip rings, and the data acquisition instrument. The uncertainties in the measurement of current (I) and voltage (V) were 2.60 % and 0.56 %, respectively. Since the thermal load (Q) was calculated as the product of I and V ($Q = I{\cdot}V$), its uncertainty was 2.66 %. Finally, based on Eqs. (1) and (2), the uncertainty in thermal conductance was determined to be 4.80 %.

3. Results and discussion

3.1. Transient characteristics

Fig. 4 illustrates the temperature variation curves of the DCCLHP with a thermal load of 250 W and a heat sink temperature of 20 ℃ for direction A and 6 g. Fig. 5 shows the transient visualization images of CC2 under the aforementioned conditions. After applying acceleration and thermal load at 300 s, the temperatures at the evaporator, CCs, vapor pipe, and condenser measurement points increased immediately. In contrast, the temperatures at LP_IN and LP_OUT on the liquid pipe decreased sequentially, reaching their lowest points of 19.8 ℃ and 21.4 ℃ at approximately 310 s and 320 s, respectively. This can be explained by the visualization in Fig. 5, which shows that the hot vapor rapidly generated in the evaporator entered the condenser through the liquid pipe, pushing the cooled liquid from the condenser back into the CCs. As a result, the temperatures at LP_IN and LP_OUT dropped. After that, when the condenser was fully filled with hot vapor, the condensation temperature increased. Fig. 5(d) shows a considerable number of

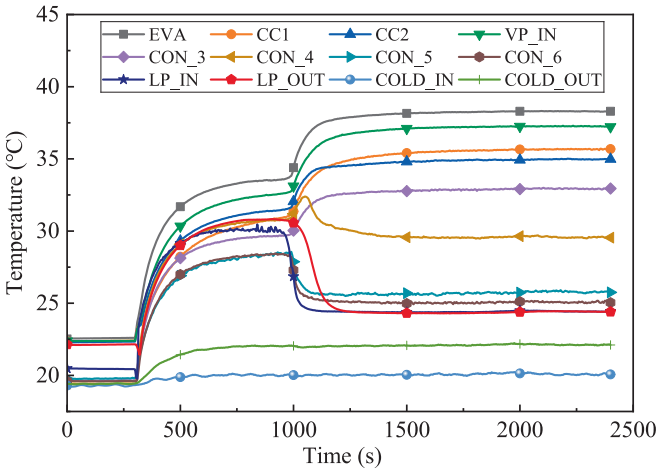

Fig. 4. Temperature variation curves of the DCCLHP at direction A and 6 g for 250 W.

bubbles entering the CC2 from the liquid pipe, indicating that a high-temperature vapor–liquid two-phase flow entered the liquid pipe. This led to the temperature increase at LP_IN and LP_OUT after approximately 310 s. By around 750 s, LP_IN and LP_OUT temperatures stabilized at about 30.1 ℃ and 30.8 ℃, while the evaporator temperature remained at 33.5 ℃. However, due to insufficient subcooling of the returning liquid into the CCs, the system at quasi-steady state required an increase in evaporator temperature to adjust the condenser outlet temperature. After 960 s, the evaporator temperature began to increase. the temperatures at LP_IN, CON_6, CON_5, and LP_OUT decrease sequentially, whereas CON_3 gradually increased and CON_4 initially increased before declining. Therefore, the vapor–liquid interface in the condenser receded between CON_4 and CON_5, and the liquid working fluid gradually filled the liquid pipe. Finally, the DCCLHP reached a steady-state operation, with the evaporator temperature at approximately 38.3 ℃.

From Fig. 5(a)–(c), it can be observed that within 20 s of applying thermal load and acceleration, the liquid in CC2 rapidly increased, and the angle of the vapor–liquid phase interface relative to the horizontal plane gradually expanded. The liquid accumulated on the side near the liquid pipe outlet under acceleration effect. The thermal load caused rapid heating and vaporization of the working fluid in the evaporator, pushing subcooled liquid from the condenser back toward the CCs. During the subsequent temperature increase at LP_IN and LP_OUT, a considerable number of bubbles were observed entering the CC2 from the liquid pipe, as illustrated in Fig. 5(d). This indicated that vapor–liquid two-phase flow occurred in both the condenser and liquid pipe, potentially responsible for the low-amplitude temperature oscillations at the LP_IN point. As the loop neared an initial steady state, bubbles ingress into the CC2 diminished significantly, as depicted in Fig. 5(e). The bubble elimination process terminated at 1330 s when the CC2 became completely bubble-free, as shown in Fig. 5(f). It also can be clearly seen from Fig. 5(e) and (f) that the vapor–liquid interfaces were almost vertical. This phenomenon occurred because the horizontal acceleration force played a dominant role at 6 g, leading to the resultant force to align predominantly with the horizontal direction. As a result, the liquid completely filled the liquid pipe and the two-phase interface in the condenser retreated between CON_4 and CON_5. These simultaneous phenomena manifested that the system attained a final steady-state operation.

Fig. 6 displays the temperature variation curves of the DCCLHP at a heat sink temperature of 20 ℃ for direction C and 15 g, with thermal loads of 50 W, 100 W, 150 W, 200 W, and 250 W. Fig. 7 shows the transient visualization images of the CC2 under the above described conditions for 50 W and 200 W. As illustrated in Fig. 6, the operational

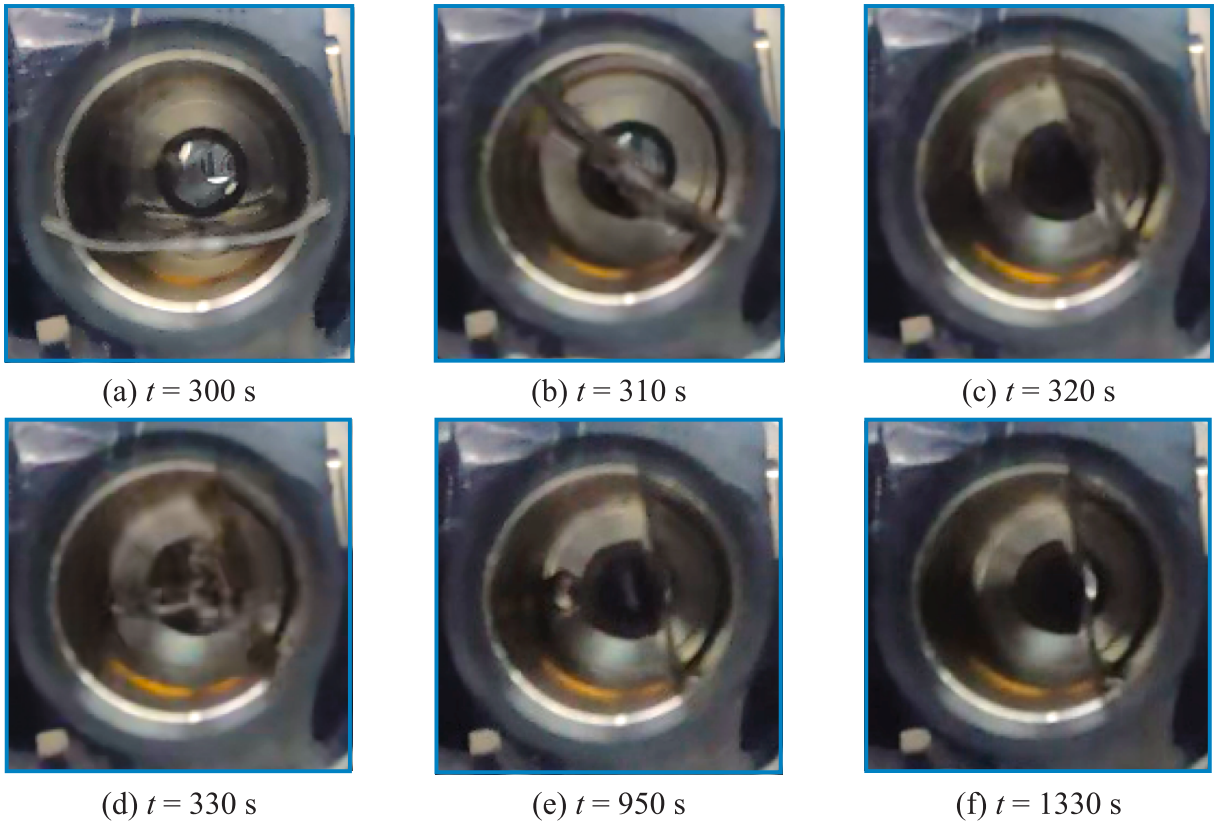

Fig. 5. Vapor-liquid distribution in the CC2 at different times under direction A and 6 g for 250 W.

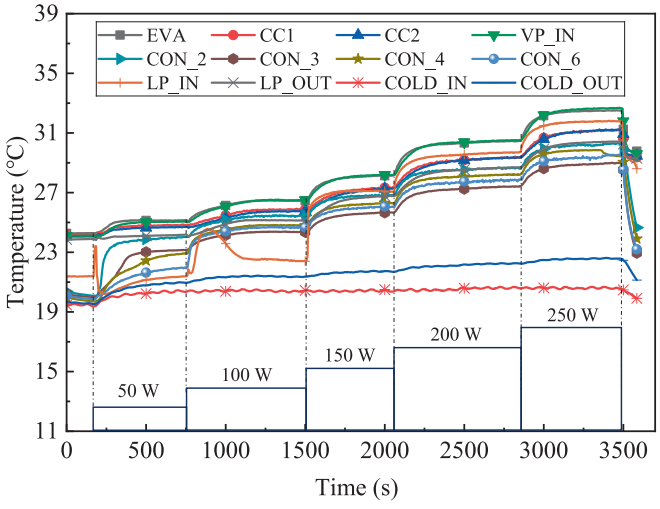

Fig. 6. Temperature variation curves of the DCCLHP at direction C and 15 g for 50 W to 250 W.

temperature progressively increased with thermal load, reaching 24.9 ℃, 26.5 ℃, 28.2 ℃, 30.5 ℃, and 32.5 ℃, respectively. Furthermore, except for the 50 W and 100 W conditions, the temperature curves of all measurement points demonstrated a gradient increase with the thermal load increasing.

Around 170 s, the application of thermal load and acceleration caused the temperatures of the evaporator, CCs, vapor pipe, condenser, and liquid pipe to start increasing, with a more significant temperature increase observed at the liquid pipe inlet. The reason could be explained that a stratified vapor–liquid two-phase flow was present in the liquid pipe. At this time, the vapor with a temperature of about 24 ℃ flowed back in reverse into the liquid pipe, leading to a rapid temperature rise at LP_IN. At approximately 185 s, the temperature at LP_IN peaked at 23.4 ℃, then quickly dropped to 20.2 ℃ before gradually increasing to approximately 21.4 ℃. The temperature at LP_OUT consistently maintained at approximately 23.8 ℃. This phenomenon was caused mainly due to the reverse flow of the vapor from the CCs to the liquid pipe. The mass flow rate of the working fluid was small at 50 W in the loop. The favorable effect of the acceleration promoted the liquid flowing into the CCs along the bottom of the liquid pipe. But the vapor reversely flowed toward the inlet along the upper part of the liquid pipe. When the DCCLHP reached a steady state at 50 W, the operational temperature stabilized at 24.9 ℃, with the temperatures at CON_2, CON_3, CON_4, CON_6, and LP_IN increasing sequentially. This indicates that the two-phase interface within the condenser was probably close to the outlet of the condenser.

When the thermal load was elevated to 100 W, the temperatures at the evaporator, CCs, vapor pipe, condenser, and liquid pipe all began to increase. The temperature at the liquid pipe inlet showed a slight fluctuation before gradually increasing to a peak of 24.5 ℃, followed by a slow decrease to approximately 22.4 ℃. The underlying reason was that the vapor with high temperature reversely reached the inlet from the outlet of the liquid pipe. Then the cool liquid from the condenser flowed into the liquid pipe. At this stage, the temperature differences across all measurement points of the condenser were within about 2 ℃.

As the thermal load increased to 150 W, the temperatures at all measurement points increased and the temperature at LP_IN neared that of the CCs. This indicated that the working fluid in both condenser and liquid pipe was in a vapor–liquid two-phase state. At 200 W and 250 W, the temperature at LP_IN exceeded that of the CCs, while both condenser and liquid pipe were also in a two-phase state. Furthermore, for thermal loads above 50 W, the temperature at CON_3 consistently remained the lowest among the measured points in the condenser. This phenomenon could be attributed to the liquid accumulation in the U-shape pipe due to

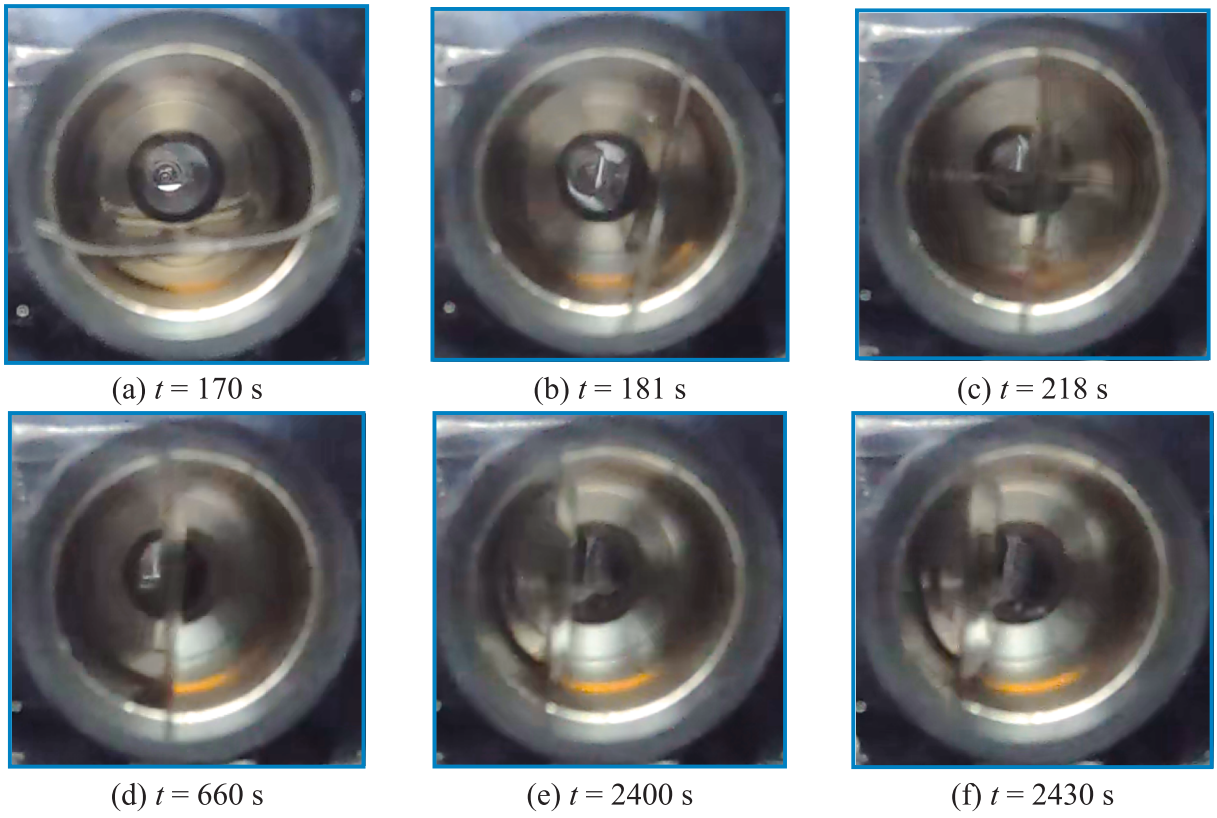

Fig. 7. Vapor-liquid distribution in the CC2 at direction C and 15 g for 50 W to 200 W.

the acceleration effect of direction C.

From Fig. 7(a)–(b), it can be observed that within 11 s after the application of acceleration and thermal load, the amount of liquid working fluid in the CC2 remained almost constant, while the angle of the two-phase interface relative to the horizontal plane gradually increased. The liquid accumulated on the side away from the liquid pipe outlet under the influence of acceleration. During this stage, stratified vapor–liquid two-phase flow was present in the liquid pipe, with vapor backflowing into the condenser and liquid flowing into the CCs due to the acceleration, causing the temperature at LP_IN to rise. Subsequently, the liquid in the condenser was rapidly transferred into the CC2, leading to an obvious liquid volume increasing in Fig. 7(c). The liquid flowing through the inlet of liquid pipe decreased the temperature at LP_IN. By 660 s, the DCCLHP had reached a stable operating state, as illustrated in Fig. 7(d). The liquid flowed into the CC2 and minimally disturbing the vapor–liquid phase interface. The amount of liquid in the CC2 further increased with thermal load elevated to 200 W, as depicted in Fig. 7(e) and (f). At this stage, the DCCLHP reached a stable operating state, but intermittent impacts of the returning working fluid on the two-phase interface in CC2 were still observed. This indicated the presence of a two-phase state in the liquid pipe, explaining the higher temperatures at LP_IN and LP_OUT seen in Fig. 6.

3.2. Impact of various factors on steady-state characteristics

3.2.1. Impact of different thermal loads

Fig. 8 illustrates the variations in the operating characteristics of the DCCLHP with increasing thermal loads under 0 g, 6 g, and 9 g for direction A, and under 6 g, 9 g, 12 g, and 15 g for direction C, all at a heat sink temperature of 20 ℃. At both directions A and C, the operational temperature generally grew with thermal load increasing. Under terrestrial gravity, the operational temperature exhibited a characteristic "V" shape across the thermal loads range of 30 ~ 300 W. For direction A at 9 g, the DCCLHP failed to operate when thermal load exceeded 100 W. In contrast, for direction C with 15 g, the DCCLHP maintained stable operation even at 400 W. For direction C, thermal conductance increased with thermal load before stabilizing at a constant value, showing a trend similar to that under terrestrial gravity. However, for direction A at 6 g, thermal conductance initially increased with increasing thermal load but subsequently decreased.

In Fig. 8(a), the operational temperature for direction A at 6 g was 28.4 ℃ at 30 W and increased with increasing thermal load, reaching a maximum of 44.9 ℃ at 300 W. For direction A at 9 g, the operational temperature started at 28.9 ℃ at 30 W and gradually increased to 38.6 ℃ at 100 W. However, when the thermal load exceeded 100 W, the DCCLHP could not operate normally. Under terrestrial gravity, the operational temperature reached 27.6 ℃ at 30 W, dropped to a minimum of 25.9 ℃ at 50 W, and then increased to 36.9 ℃ at 300 W. These findings indicate that at direction A under 6 g and 9 g, the operational temperatures were higher compared to terrestrial gravity, with the 9 g condition resulting in higher temperature than the 6 g condition.

In Fig. 8(b), the operational temperature curves at 6 g, 9 g, 12 g, and 15 g were highly consistent across the 100 ~ 400 W range. However, the overall operational temperature was slightly lower at 15 g. For direction C at 6 g and 12 g, the operational temperatures were 26.0 ℃ and 26.6 ℃ at 50 W, respectively, and showed a slight decrease to their minimum values of 25.7 ℃ and 26.0 ℃ at 100 W before increasing with higher thermal loads. The lowest temperature recorded was 24.9 ℃ at 15 g and 50 W. By contrast, the highest temperature reached 40.2 ℃ at 6 g and 400 W. Additionally, it is worth pointing out that the operating temperature profile predominantly exhibits a "/" shape oblique line, deviating from the conventional "V" shape curve. The reason can be addressed as follows: The additional pressure head generated by the acceleration force enhanced rather than resisted the liquid working fluid flowing back to the CCs. Correspondingly, the total pressure drop of the external loop decreased. At low thermal loads, the subcooling of the returning liquid is sufficient to balance the heat leakage, resulting in a low operational temperature. At high thermal loads, the subcooling of

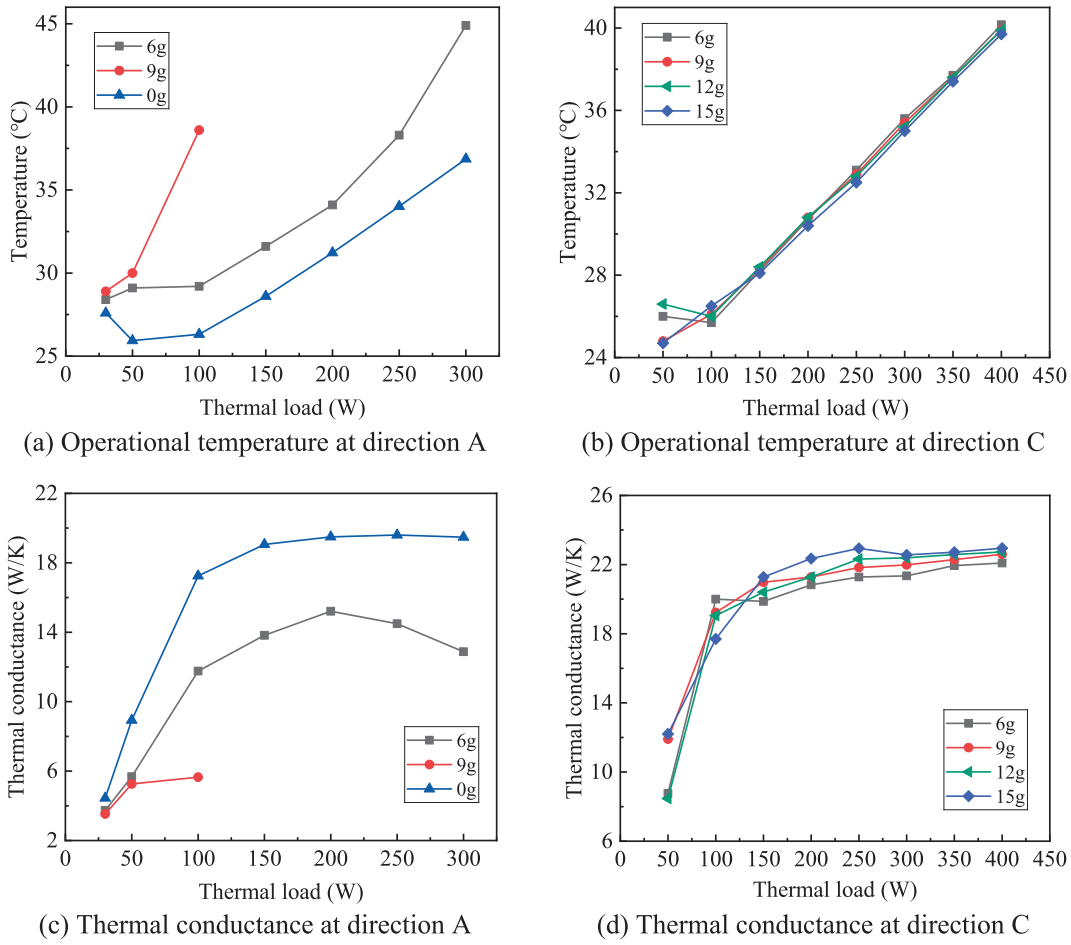

Fig. 8. Operating performance versus thermal loads at directions A and C.

the liquid exiting the condenser also dominates the operational temperature, which increases almost linearly with the thermal load. Therefore, the operational temperature exhibits a "/" shape oblique line.

In Fig. 8(a) and (b), the operational temperature increased with thermal loads above 100 W at directions A and C. The underlying mechanism can be addressed as follows. An increase in thermal load elevated the evaporation rate of the liquid in the evaporator, leading to higher flow resistance and pressure drop of the loop. Thus, the capillary force enhanced to compensate the pressure drop by reducing the curvature radius of the meniscus. Moreover, as the total pressure drop increased, the pressure differential between the vapor–liquid phase interface in the CCs and the meniscus grew accordingly. According to the Clausius-Clapeyron equation (Eq. (4)) [8,56], it elevated the temperature difference between the evaporator and the CCs. Correspondingly, the greater heat leakage from the evaporator to the CCs was produced, thereby increasing the operational temperatures.

$$\Delta p = \left(\frac{dp}{dT}\right)_{sat} \cdot \Delta T = \frac{h}{T_{sat} v_{vl}} \cdot \Delta T \tag{4}$$

where Δp is the total pressure drop excluding the pressure drop in capillary wick, dp/dT is the slope of the ammonia saturation pressure–temperature curve, ΔT is the temperature difference between the evaporator and the CCs, h is the latent heat of the working fluid, T_{sat} is the saturation temperature, and v_{vl} is the difference in specific volume between the saturated vapor and saturated liquid.

In Fig. 8(c), under terrestrial gravity, thermal conductance consistently increased with thermal load and remained within the range of 19.06 W/K to 19.60 W/K above 150 W. For direction A at 9 g, the thermal conductance increased from 3.53 W/K at 30 W to 5.65 W/K at 100 W. Under the 6 g condition, thermal conductance reached its lowest value of 3.73 W/K at 30 W, then increased with increasing thermal load, peaking at 15.21 W/K at 200 W before declining to 12.88 W/K at 300 W. The reasons for this change can be explained as follows. Under the influence of adverse-direction acceleration, the liquid returning encountered obviously elevated flow resistance. When the thermal load exceeded a critical value, the heat leakage increased rapidly while the subcooling of the returning liquid was limited. Consequently, the operational temperature increased rapidly, leading to the observed decrease in thermal conductance according to Eq. (2). For the same thermal load, thermal conductance decreased sequentially under terrestrial gravity, 6 g, and 9 g, with the lowest value of 3.53 W/K observed at 30 W under the 9 g condition.

In Fig. 8(d), thermal conductance increased with thermal load under all four acceleration magnitudes and gradually approached a constant value. Overall, the thermal conductance at 15 g was slightly higher than at other magnitudes. The lowest thermal conductance was 8.47 W/K at 50 W and 12 g, while the highest was 22.94 W/K at 250 W and 15 g. Additionally, thermal conductance at 9 g in direction A was consistently lower than at 6 g to 15 g in direction C.

References [57,58] present the performance of an ammonia-charged DCCLHP with a bayonet operating in acceleration environment. For the most adverse direction A, the DCCLHP could operate normally at 7 g and 300 W. In the current work, the proposed DCCLHP could maintain normal operation under adverse direction A at 6 g with a thermal load of 300 W or higher. For direction C, the proposed DCCLHP demonstrated comparable operational performance to the previous DCCLHP design. Particularly at direction D, it exhibited lower operational temperature and higher thermal conductance.

Moreover, compared to the DCCLHPs with an extended bayonet [24] or dual bayonets [25], the proposed DCCLHP successfully achieved startup and stable operation under adverse direction A at 9 g and a low thermal load of 30 W. Notably, in terrestrial gravity environment, the system thermal resistance of the current design (0.051 K/W at 200 W) was lower than the minimum thermal resistance (0.067 K/W) reported for the dual-bayonet DCCLHP.

3.2.2. Impact of different acceleration directions

Fig. 9 displays the operational temperature and thermal conductance of the DCCLHP in four typical directions A, B, C, and D under a heat sink temperature of 20 ℃. The relevant acceleration magnitudes and thermal loads were 3 g and 150 W, 6 g and 150 W, 12 g and 150 W, and 12 g and 200 W, respectively. Notably, the DCCLHP failed to operate at direction A under 12 g with 150 W and 200 W. The highest operational temperature and lowest thermal conductance were observed in direction B under identical conditions, whereas the lowest operational temperature and highest thermal conductance occurred in direction D under different conditions. Specifically, the lowest thermal conductance of 13.22 W/K was recorded at 12 g and 150 W in direction B, while the lowest operational temperature of 27.8 ℃ was achieved at 3 g and 150 W in direction D.

In Fig. 9(a), for direction A and 150 W, the DCCLHP exceeded its allowable operational temperature when the acceleration was greater than 6 g. Specifically, at 12 g and 150 W, direction B recorded the highest operational temperature of 32.7 ℃. For directions A, B, C, and D, the operational temperatures at 3 g and 150 W were 28.6 ℃, 28.5 ℃, 28.1 ℃, and 27.8 ℃, respectively. For directions B, C, and D, the operational temperatures at 12 g and 200 W were 30.8 ℃, 30.8 ℃, and 30.3 ℃, respectively. With the exception of the 12 g and 150 W condition, the operational temperature showed minor differences for directions B, C, and D. Overall, the operational temperature decreased sequentially from directions A to D across these conditions. This indicated that the acceleration effects in directions C and D positively influenced the loop operation.

In Fig. 9(b), under the same operating conditions, the thermal conductance increased sequentially from directions A to D. Specifically, the thermal conductance for directions C and D was generally higher than for direction B at 12 g and 150 W. The thermal conductance for direction A was 18.63 W/K and 13.82 W/K, respectively, under 3 g and 6 g with 150 W. The highest thermal conductance of 23.12 W/K was observed at 12 g and 200 W in direction D. Notably, for direction D and 150 W, the thermal conductance at 3 g was slightly higher than at 6 g, which differed from the trends observed at directions B and C.

Different acceleration directions could influence the two-phase distribution and changed the flow resistance in the loop, thereby affecting its total pressure drop. The additional flow resistance induced by acceleration was represented by an additional pressure head, as formulated in Eq. (5).

$$\Delta p_a = \rho a L \tag{5}$$

Where L is the effective liquid length along the acceleration direction, ρ is the density of the liquid or vapor working fluid, and a is the acceleration magnitude.

In the current work, the gravitational contribution to pressure drop remained negligible due to the horizontal arrangement of the loop. However, the additional pressure head was favorable when acceleration was aligned with the flow direction. Otherwise, it created the flow resistance.

Since this DCCLHP did not have a bayonet, the total pressure drop of the entire loop in this experiment could be calculated according to Eq. (6) [59].

$$\Delta p_{tot} = \Delta p_{vg} + \Delta p_{vp} + \Delta p_c^1 + \Delta p_c^2 + \Delta p_{lp} + \Delta p_a + \Delta p_w \tag{6}$$

where Δp_{vg} and Δp_{vp} are the pressure drops through the vapor groove and vapor pipe, respectively. Δp_c^1 and Δp_c^2 are the pressure drops of the single-phase and two-phase flows through the condenser, respectively. Δp_w is the pressure drop through the capillary wick, and Δp_{lp} is the working fluid pressure drop in the liquid pipe. Under normal operating conditions, both the mass flow rate and two-phase region length contribute to increases in Δp_c^1, Δp_c^2 and Δp_{lp} values.

Notably, the acceleration mainly affected the pressure drop in the liquid pipe and condenser, but its effect on the vapor transport components remained negligible due to the significantly lower vapor density. To maintain force balance, the capillary wick adaptively adjusts the meniscus radius to generate the driving force necessary for the normal operation of the system.

At 3 g with 150 W, the acceleration direction A was opposite to the flow direction of the liquid in the liquid pipe. The additional pressure head caused a sharp increase in the loop pressure drop, which led to a significant temperature difference between the evaporator and the CCs. Therefore, the DCCLHP was prone to exceeding its normal operational temperature. For direction B, based on the transient temperature variation curve under this condition, the two-phase interface of the working fluid in the condenser was between CON_4 and CON_6. The driving force was generated in the condenser to reduce the total pressure drop. Fig. 10 schematically illustrates the vapor–liquid phase distribution at directions C and D, which could help in finding the vapor–liquid interface position in an approximate manner. It should be noted that it is difficult

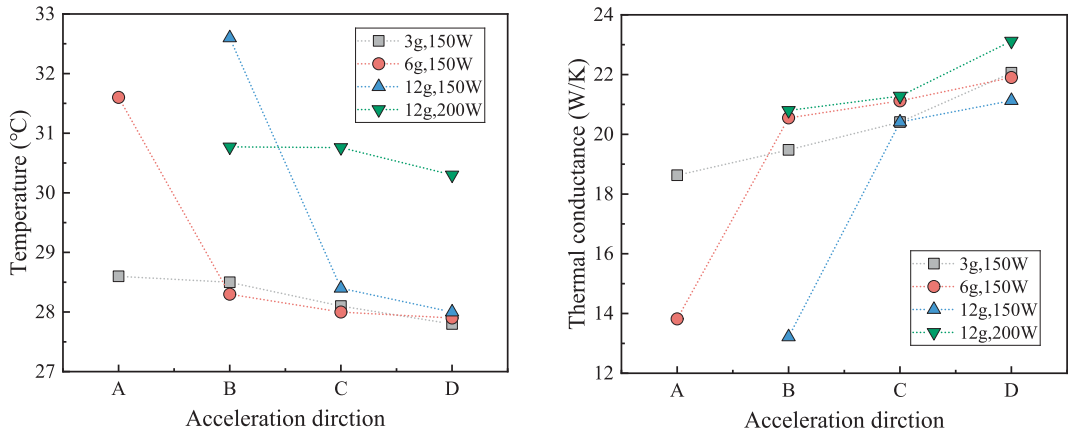

(a) Operational temperature (b) Thermal conductance

Fig. 9. Operating performance versus four acceleration directions under specific conditions.

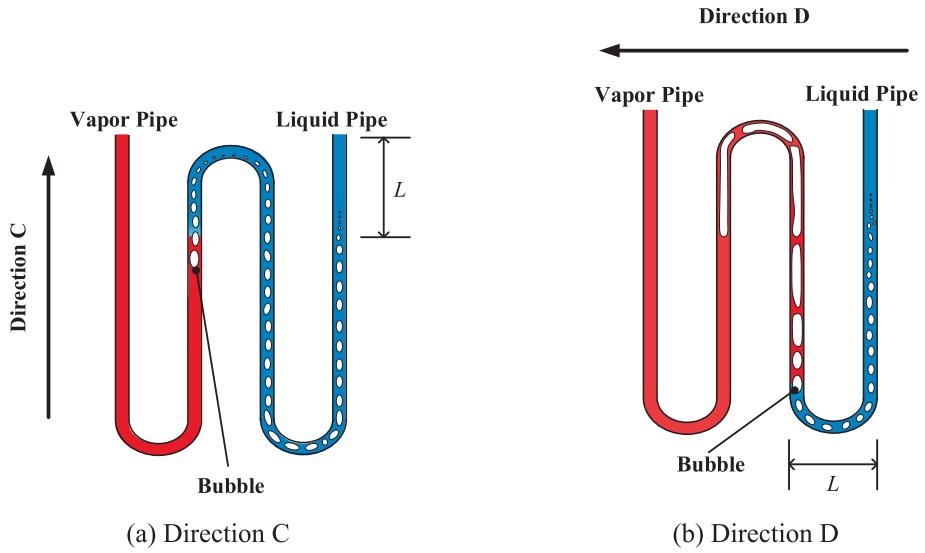

(a) Direction C (b) Direction D

Fig. 10. Schematic diagram of the vapor–liquid interface position in the condenser at 3 g with 150 W.

to accurately determine the vapor–liquid interface position due to the complexity of vapor–liquid two-phase flow. For direction C, the two-phase interface in the condenser was approximately between CON_6 and the outlet of the condenser, as shown in Fig. 10(a). The acceleration direction aligned with the working fluid flow direction in the liquid pipe, generating a driving force. Furthermore, a greater favorable additional pressure head for direction C was resulted from the longer effective liquid flow length in the loop compared to direction B, further promoting a lower operational temperature and higher thermal conductance, as shown in Fig. 9. For direction D, the two-phase interface in the condenser was approximately near the outlet of the condenser, as shown in Fig. 10(b). The acceleration effect generated relatively small flow resistance in the condenser but a larger driving force in the evaporator core. Thus, direction D may achieve a lower operational

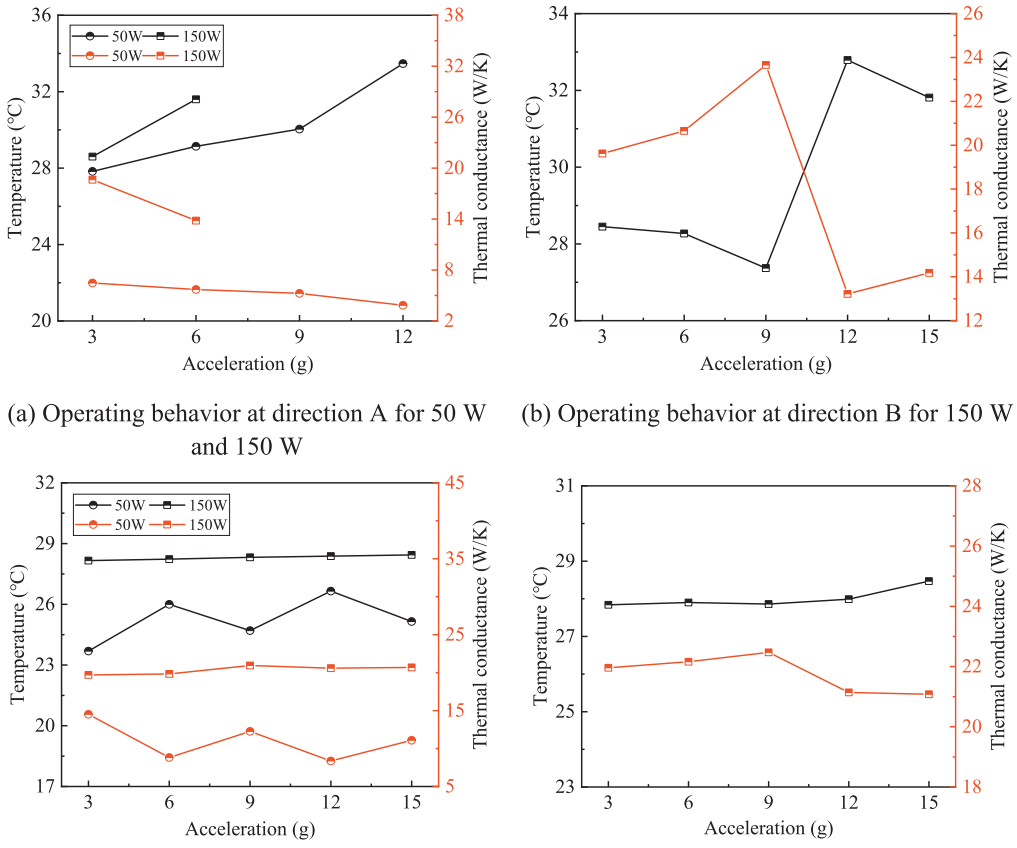

(a) Operating behavior at direction A for 50 W and 150 W

(b) Operating behavior at direction B for 150 W

(c) Operating behavior at direction C for 50 W and 150 W

(d) Operating behavior at direction D for 150 W

Fig. 11. Operating behavior versus acceleration magnitudes at different thermal loads and directions.

temperature and higher thermal conductance than those for direction C, which differs from the experimental results in Ref. [52]. Therefore, under most operating conditions in this experiment, the superior performance observed at direction D was attributed to a combination of factors, including the acceleration effect, the system structure, and the vapor–liquid phase distribution of the working fluid.

3.2.3. Impact of different acceleration magnitudes

Fig. 11 depicts the operational temperature and thermal conductance of the DCCLHP under accelerations in directions A, B, C, and D and a heat sink temperature of 20 ℃, varying with acceleration magnitude. The thermal load was 50 W and 150 W. The acceleration range was from 3 g to 15 g for directions B, C, and D, whereas the maximum acceleration was limited to 12 g for direction A.

In Fig. 11(a), when the thermal load was 150 W and the acceleration exceeded 6 g for direction A, the evaporator temperature increased too high to achieve a stable state. For both thermal loads, the operational temperature increased with acceleration magnitude, while thermal conductance decreased. The reason could be that the additional pressure head induced by the acceleration increased with the acceleration magnitude increasing according to Eq. (5). It led to the larger pressure drop of the loop and more significant temperature difference between the evaporator and the CCs. Consequently, the larger operational temperature was produced. Accordingly, the thermal conductance decreased by Eq. (2). The lowest and highest operational temperatures at 50 W were 27.8 ℃ and 33.5 ℃, corresponding to acceleration magnitudes of 3 g and 12 g, respectively. The lowest thermal conductance, 3.84 W/K, occurred at 50 W and 12 g, whereas the highest thermal conductance, 18.63 W/K, was observed at 150 W and 3 g.

It can be also clearly seen from Fig. 11(a) that the operational temperature at 50 W increased more rapidly with acceleration increasing from 9 g to 12 g compared to the range from 3 g to 9 g. Correspondingly, the thermal conductance decreased more rapidly with increasing acceleration. This indicates that higher acceleration magnitudes further deteriorate the operational performance of the DCCLHP. Additionally, the operational temperature at 150 W increased more rapidly compared to that at 50 W, with acceleration increasing from 3 g to 6 g, and the thermal conductance decreased more significantly. This suggests that at lower thermal loads, the operational performance at direction A is less sensitive to changes in acceleration magnitude.

In Fig. 11(b), the operational temperature at direction B initially decreased with increasing acceleration, then increased, and subsequently decreased again. Conversely, the thermal conductance exhibited the opposite pattern. This indicated that increasing acceleration within a certain range could enhanced the operational performance at direction B. However, once a specific threshold was exceeded, the operational temperature increased significantly. Specifically, the operational temperature reached its lowest value of 27.4 ℃ at 9 g and its highest value of 32.7 ℃ at 12 g. Correspondingly, the thermal conductance peaked at 23.66 W/K at 9 g and dropped to its lowest value of 13.22 W/K at 12 g.

In Fig. 11(c), the operational temperature at 150 W increased with acceleration to a lesser extent compared to that at 50 W for direction C. At a constant acceleration magnitude, both operational temperature and thermal conductance were higher at 150 W than at 50 W. At 50 W, the operational temperature reached its lowest value of 23.7 ℃ at 3 g and its highest value of 26.6 ℃ at 12 g. Correspondingly, the thermal conductance was lowest at 12 g (8.47 W/K) and highest at 3 g (14.51 W/K). Overall, under these conditions, the operational temperature increased with acceleration, while the thermal conductance decreased. For 150 W, the operational temperature gradually increased with increasing acceleration, ranging from a minimum of 28.2 ℃ at 3 g to a maximum of 28.4 ℃ at 15 g, showing a slight temperature difference of only 0.2 ℃. The thermal conductance was lowest at 3 g (19.69 W/K) and highest at 9 g (20.94 W/K), showing a slight overall increase with acceleration. According to Fig. 8(b), the operational temperature at direction C slightly decreased with increasing acceleration, when thermal load exceeded 200 W. These observations highlighted that the operating behavior for this DCCLHP was influenced by multiple factors rather than a single determinant.

In Fig. 11(d), the operational temperature at direction D increased slightly with acceleration, whereas the thermal conductance manifested a declining tendency. The lowest operational temperature was 27.8 ℃ at 3 g, while the highest was 28.5 ℃ at 15 g. The thermal conductance reached its minimum of 21.08 W/K at 15 g and its maximum of 22.47 W/K at 9 g. Notably, the thermal conductance initially increased slightly from 3 g to 9 g, but then decreased with further increases in acceleration. The difference between the maximum and minimum operational temperatures was only 0.7 ℃, and the difference in thermal conductance was 1.39 W/K. These minimal variations indicated that the DCCLHP operated stably at direction D with 150 W, showing low sensitivity to change in acceleration magnitude.

3.2.4. Impact of different heat sink temperatures

Fig. 12 displays the variations in operational temperature and thermal conductance under 12 g and 150 W for directions B and C, with heat sink temperature increasing from 10 ℃ to 25 ℃. It can be clearly seen that both operational temperature and thermal conductance for the two directions gradually increased with increasing heat sink temperature. In addition, the rate of increase with heat sink temperature was similar. However, the thermal conductance at direction C increased at a slightly faster rate compared to direction B. Notably, direction B showed consistently higher operational temperature and reduced thermal conductance compared to direction C under identical heat sink temperature and thermal load conditions. This indicated that direction C was more favorable for maintaining stable and efficient operation. The maximum temperature for direction B was 35.7 ℃ at a heat sink temperature of 25 ℃, while the minimum temperature for direction C was 22.3 ℃ at 10 ℃. Additionally, the thermal conductance for direction C peaked at 21.40 W/K at a heat sink temperature of 25 ℃, while the thermal conductance for direction B reached a minimum of 12.12 W/K at 10 ℃.

For the same thermal load, the evaporation rate of the liquid working fluid in the evaporator remains constant. However, as the heat sink temperature increased, the cooling efficiency of the condenser dropped. It caused two phase zone remain uncondensed, further resulting in an increase in condenser pressure drop. According to Eq. (4), an increase in the temperature difference (ΔT) between the evaporator and the CCs corresponded to a rise in the evaporator temperature. Under constant thermal load conditions, the thermal conductance presented a positive correlation with heat sink temperature. This behavior manifested as a

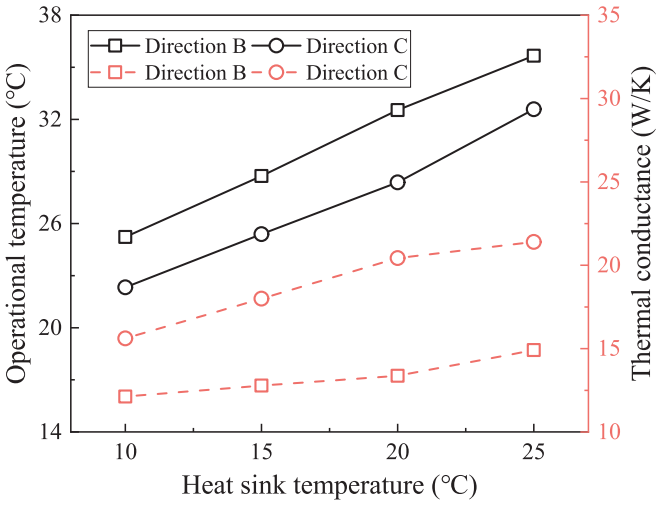

Fig. 12. Operating behavior versus heat sink temperature for directions B and C at 12 g with 150 W.

reduction in the temperature difference between the evaporator and condenser with increasing heat sink temperature, consequently causing an increase in thermal conductance. Although elevated heat sink temperature induced the increase in electronic device operating temperature, it also significantly enhanced thermal conductance. Therefore, in practical applications, the heat sink temperature can be suitably increased to ensure the proper functioning of both the electronic devices and the DCCLHP, balancing operational temperature and thermal performance.

Fig. 13 illustrates the variations in steady-state temperatures at the vapor pipe outlet (VP_OUT), liquid pipe inlet (LP_IN), and multiple points along the condenser with the heat sink temperature increasing at 12 g and 150 W in direction C.

According to Fig. 13, it can be observed that the temperatures of all measurement points gradually increased with the rise in heat sink temperature. However, there was no significant temperature difference between different measurement points, indicating that the working fluid remained in a two-phase state within the condenser. At a heat sink temperature of 10 ℃, CON_1 and CON_5 recorded the highest temperatures among all measurement points, at 21.9 ℃ and 22.0 ℃, respectively, while CON_3 had the lowest temperature in the condenser, at 19.5 ℃. This suggests that the vapor-phase working fluid primarily accumulated at one end of the condenser, opposite to the acceleration direction C. As the heat sink temperature increased, CON_1 and CON_5 became the lowest temperature points, at 28.5 ℃ and 28.3 ℃, respectively, when the heat sink temperature reached 25 ℃. In contrast, CON_3 showed a temperature of 29.0 ℃. This indicates that the vapor-phase working fluid no longer accumulated at a specific end of the condenser due to the acceleration effect. Furthermore, with heat sink temperature increasing to 20 °C and 25 °C, the temperature of LP_IN exceeded that of all monitoring points on the condenser, and the liquid pipe evolved into a coexisting vapor and liquid phase state. These observations highlight that the heat sink temperature significantly influenced the two-phase flow and distribution of the working fluid through the condenser. Higher heat sink temperature can extend two-phase region, and increase the flow resistance of the external loop, thereby affecting the operating behavior.

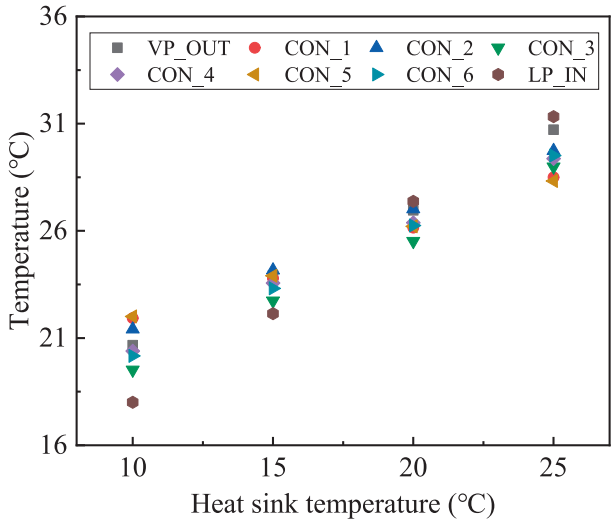

Fig. 13. Temperature of condenser versus heat sink temperature at 12 g with 150 W for direction C.

4. Conclusions

This study presents an experimental investigation of a newly designed visual ammonia-charged dual compensation chamber loop heat pipe (DCCLHP) without a bayonet, focusing on its performance under high acceleration conditions. The impacts of several key operational parameters, including thermal load, magnitude and direction of acceleration, and heat sink temperature, were systematically examined. The main findings are summarized as follows:

(1) Under high acceleration conditions, an increase in thermal load can elevate the operational temperature. For direction C, the operating temperature profile primarily follows a "/" shape oblique trend. The thermal conductance gradually increases and stabilizes at a certain value. Larger thermal load can lead to thermal conductance declining. Moreover, the system without a bayonet can operate normally at 300 W and 6 g in the most adverse direction A and achieving successful startup at 30 W and 9 g.
(2) For the four directions from A to D, the operational temperature decreases and the thermal conductance increases sequentially. Direction A significantly deteriorates operational performance, whereas direction D achieves lower operational temperature and higher thermal conductance. Specifically, for 3 g and 150 W, the operational temperature is 27.8 ℃; and for 12 g and 200 W, the thermal conductance reached 23.12 W/K.
(3) Vapor-liquid two-phase flow can simultaneously exist within the liquid pipe and condenser at high thermal loads. And the loop can operate to a steady state after the vapor–liquid phase redistribution. Vapor backflow may occur during startup for direction C and the liquid pipe contains stratified two-phase fluid.
(4) As acceleration increases, the operational temperature increases and thermal conductance decreases for direction A. The operational temperature first decreases, then increases, and decreases again for direction B, with thermal conductance showing the opposite trend. At directions C and D, the operational temperature increases, and thermal conductance may either increase or decrease, related to the thermal load.
(5) Higher heat sink temperature increases both operational temperature and thermal conductance. Concomitantly, it can extend the two-phase region within the condenser and even result in the liquid pipe transitioning to a vapor–liquid two-phase state.

In this study, we visually observed and manifested the heat transfer and two-phase flow behaviors of the DCCLHP without a bayonet in high acceleration environment up to 15 g, which are the critical considerations in practical applications. The corresponding interpretation and underlying physical mechanism explanation are proposed for the first time. The newly designed DCCLHP still exhibits excellent operational performance even under challenging conditions of adverse acceleration orientation and low heat loads. These findings provide theoretical validation for implementing this advanced DCCLHP design in thermal management systems for onboard electronic devices.

CRediT authorship contribution statement

Yongqi Xie: Writing – original draft, Supervision, Funding acquisition, Formal analysis, Conceptualization. **Lijun Chen:** Methodology, Formal analysis, Data curation. **Jiayi Bao:** Supervision, Project administration, Methodology, Conceptualization. **Huifeng Kang:** Resources, Investigation, Data curation. **Zhen Fang:** Visualization, Investigation, Formal analysis. **Hongwei Wu:** Writing – review & editing, Supervision, Conceptualization.

Declaration of competing interest

The authors declare that they have no known competing financial interests or personal relationships that could have appeared to influence the work reported in this paper.

Acknowledgment

The authors acknowledge the financial supports from National Natural Science Foundation of China (No. 12272027).

Data availability

Data will be made available on request.

References

[1] C. Chen, Y. Liu, J. Li, et al., Flow and heat transfer characteristics of manifold microchannels with different microchannel arrangements, Therm. Sci. Eng. Prog. (2025) 103354.
[2] C. Suresh, A. Awasthi, B. Kumar, et al., Advances in battery thermal management for electric vehicles: a comprehensive review of hybrid PCM-metal foam and immersion cooling technologies, Renew. Sustain. Energy Rev. 208 (2025) 115021.
[3] D. Ni, F. Yu, CFD simulation study of flow equalisation plate model in single-phase immersion liquid cooling for servers, Therm. Sci. Eng. Prog. 47 (2024) 102268.
[4] B. Xu, J. Chang, M. Wu, et al., Flow and heat transfer characteristics of spray cooling on hydrophilic-hydrophobic mixed surface under heterogeneous heat sources, Therm. Sci. Eng. Prog. 60 (2025) 103442.
[5] X. Liu, L. Liu, R. Li, et al., Research on the performance and application of spray cooling in the gas phase space, Therm. Sci. Eng. Prog. (2025) 103383.
[6] S.W. Chang, W.L. Cai, Thermal impact of integrated bore cooling with impinging jets and turbulators in rotating shaft of interior permanent magnet electric motor, Therm. Sci. Eng. Prog. 57 (2025) 103164.
[7] T. Idris, W.M. El-Maghlany, M. Elhelw, et al., Thermo-electro-hydraulic performance of jet impingement on solar photovoltaic integrated with absorber fins, Therm. Sci. Eng. Prog. 57 (2025) 103158.
[8] Y.F. Maydanik, Loop heat pipes, Appl. Therm. Eng. 25 (5–6) (2005) 635–657.
[9] L. Bai, J. Fu, G. Lin, et al., Quiet power-free cooling system enabled by loop heat pipe, Appl. Therm. Eng. 155 (2019) 14–23.
[10] C. Nashine, M. Pandey, K.K. Baraya, Experimental studies on the transient characteristics and start-up behavior of a miniature loop heat pipe, Appl. Therm. Eng. 259 (2025) 124814.
[11] Y. Zhang, G. Wang, X. Wang, et al., Performance and energy consumption study of a dual-evaporator loop heat pipe for chip-level cooling, Appl. Therm. Eng. 258 (2025) 124757.
[12] C. Zilio, G. Righetti, S. Mancin, et al., Active and passive cooling technologies for thermal management of avionics in helicopters: Loop heat pipes and mini-Vapor Cycle System, Therm. Sci. Eng. Prog. 5 (2018) 107–116.
[13] H. Wang, G. Lin, H. Qin, et al., Design and experimental validation of a high capacity loop heat pipe for avionics cooling, Therm. Sci. Eng. Prog. 45 (2023) 102139.
[14] Chen Y, Groll M, Mertz R, et al. Steady-state and transient performance of a miniature loop heat pipe, International Conference on Nanochannels, Microchannels, and Minichannels. 2005, 41855: 183-189.
[15] K.L. Yerkes, J. Scofield, D. Courson, Performance of a loop heat pipe subjected to a phase-coupled heat input to an acceleration field, 46th AIAA Thermophysics Conference (2016:) 4145.
[16] Gerhart C, Gluck D. Summary of operating characteristics of a dual compensation chamber loop heat pipe in gravity, 11th International Heat Pipe Conference, Tokyo, Japan. 1999.
[17] D. Gluck, C. Gerhart, S. Stanley, Characterization of a high capacity, dual compensation chamber loop heat pipe, AIP Conference Proceedings American Institute of Physics 458 (1) (1999) 943–948.
[18] S. Van Oost, B. Mullender, G. Bekaert, et al., Secondary wick operation principle and performance mapping in LHP and FLHP evaporators, AIP conference proceedings American Institute of Physics 608 (1) (2002) 94–103.
[19] A.A. Adoni, A. Ambirajan, V.S. Jasvanth, et al., Effects of mass of charge on loop heat pipe operational characteristics, J. Thermophys Heat Transfer 23 (2) (2009) 346–355.
[20] G. Lin, H. Zhang, X. Shao, et al., Development and test results of a dual compensation chamber loop heat pipe, J. Thermophys Heat Transfer 20 (4) (2006) 825–834.
[21] L. Bai, G. Lin, D. Wen, et al., Experimental investigation of startup behaviors of a dual compensation chamber loop heat pipe with insufficient fluid inventory, Appl. Therm. Eng. 29 (8–9) (2009) 1447–1456.
[22] J. Feng, G. Lin, L. Bai, Experimental investigation on operating instability of a dual compensation chamber loop heat pipe, Sci. China Ser. E: Technol. Sci. 52 (8) (2009) 2316–2322.
[23] Q. Su, S. Chang, M. Song, et al., An experimental study on the heat transfer performance of a loop heat pipe system with ethanol-water mixture as working fluid for aircraft anti-icing, Int. J. Heat Mass Transf. 139 (2019) 280–292.
[24] L. Bai, Y. Tao, Y. Guo, et al., Startup characteristics of a dual compensation chamber loop heat pipe with an extended bayonet tube, Int. J. Heat Mass Transf. 148 (2020) 119066.
[25] L. Bai, J. Fu, L. Pang, et al., Experimental study on a dual compensation chamber loop heat pipe with dual bayonet tubes, Appl. Therm. Eng. 180 (2020) 115821.
[26] P. Yang, T. Yang, T. Gao, et al., Experimental study on a dual compensation chamber loop heat pipe with a ceramic wick, Appl. Therm. Eng. 230 (2023) 120750.
[27] J. Fu, L. Bai, Y. Zhang, et al., Experimental study on the thermal performance of a dual compensation chamber loop heat pipe with dual vapor and condenser lines, Therm. Sci. Eng. Prog. 43 (2023) 101994.
[28] J. Fu, L. Bai, Y. Zhang, et al., Improved startup performance of a dual compensation chamber loop heat pipe by sequential cooling to the compensation chambers, Int. J. Heat Mass Transf. 233 (2024) 126046.
[29] H. Wang, G. Lin, Y. Guo, et al., Experimental study of a high-capacity dual compensation chamber loop heat pipe at different orientations, Int. J. Therm. Sci. 202 (2024) 109051.
[30] H. Wang, G. Lin, Y. Guo, et al., Experimental investigation on the performance of a high capacity dual compensation chamber loop heat pipe under the effect of acceleration, Case Stud. Therm. Eng. 61 (2024) 105013.
[31] Y. Xie, X. Li, L. Han, et al., Experimental study on operating characteristics of a dual compensation chamber loop heat pipe in periodic acceleration fields, Appl. Therm. Eng. 176 (2020) 115419.
[32] X. Lv, Y. Xie, H. Zhang, et al., Temperature oscillation of a dual compensation chamber loop heat pipe under acceleration conditions, Appl. Therm. Eng. 198 (2021) 117450.
[33] Y. Zhang, T. Luan, H. Jiang, et al., Visualization study on start-up characteristics of a loop heat pipe with a carbon fiber capillary wick, Int. J. Heat Mass Transf. 169 (2021) 120940.
[34] S.C. Zhao, Z.K. Zhang, R.Z. Zhao, et al., Experimental study on global visualization of loop heat pipe with a flat disk-shaped evaporator, Energy Rep. 8 (2022) 10895–10912.
[35] X. Wang, J. Yang, Q. Wen, et al., Visualization study of a flat confined loop heat pipe for electronic devices cooling, Appl. Energy 322 (2022) 119451.
[36] S. Du, Q. Zhang, L. Ling, et al., Visualization investigation on temperature oscillation and two-phase behaviors of a flat loop heat pipe, J. Therm. Sci. 32 (4) (2023) 1536–1546.
[37] J.M. Cimbala, J.S. Brenizer, A.P.Y. Chuang, et al., Study of a loop heat pipe using neutron radiography, Appl. Radiat. Isot. 61 (4) (2004) 701–705.
[38] P.Y.A. Chuang, J.M. Cimbala, J.S. Brenizer, Experimental and analytical study of a loop heat pipe at a positive elevation using neutron radiography, Int. J. Therm. Sci. 77 (2014) 84–95.
[39] A. Okamoto, R. Hatakenaka, M. Murakami, Visualization of a loop heat pipe using neutron radiography, Heat Pipe Sci. Technol. Int. J. 2 (1–4) (2011).
[40] G. Lin, N. Li, L. Bai, et al., Experimental investigation of a dual compensation chamber loop heat pipe, Int. J. Heat Mass Transf. 53 (15–16) (2010) 3231–3240.
[41] Y. Zhao, S. Chang, B. Yang, et al., Experimental study on the thermal performance of loop heat pipe for the aircraft anti-icing system, Int. J. Heat Mass Transf. 111 (2017) 795–803.
[42] M. Nishikawara, K. Otani, Y. Ueda, et al., Liquid–vapor phase behavior and operating characteristics of the capillary evaporator of a loop heat pipe at start-up, Int. J. Therm. Sci. 129 (2018) 426–433.
[43] Y. Yamada, M. Nishikawara, H. Yanada, et al., Predicting the performance of a loop heat pipe considering evaporation from the meniscus at the three-phase contact line, Therm. Sci. Eng. Prog. 11 (2019) 125–132.
[44] M. Nishikawara, S. Tomita, H. Yokoyama, et al., Relationship between phase distribution and heat-transfer coefficient of loop heat pipe evaporator investigated by lateral observation of porous media, Appl. Therm. Eng. 236 (2024) 121524.
[45] X. Chang, N. Watanabe, H. Nagano, Visualization study of a loop heat pipe with two evaporators and one condenser under gravity-assisted condition, Int. J. Heat Mass Transf. 135 (2019) 378–391.
[46] X. Chang, N. Watanabe, H. Nagai, et al., Visualization of thermo-fluid behavior of loop heat pipe with two evaporators and one condenser under various orientation with even heat loads, Int. J. Heat Mass Transf. 198 (2022) 123397.
[47] X. Chang, N. Watanabe, H. Nagai, et al., Visualization of thermo-fluid behavior of loop heat pipe with two evaporators and one condenser under various orientations with uneven heat loads, Int. J. Heat Mass Transf. 221 (2024) 125054.
[48] Q. Zhang, G. Lin, X. Shen, et al., Visualization study on the heat and mass transfer in the evaporator-compensation chamber of a loop heat pipe, Appl. Therm. Eng. 164 (2020) 114472.
[49] L. Liu, X. Yang, B. Yuan, et al., Investigation of temperature oscillations in a novel loop heat pipe with a vapor-driven jet injector, Int. J. Heat Mass Transf. 179 (2021) 121672.
[50] K. Yan, N. Li, R. Zhao, et al., Visualization study on the condensation in a propylene loop heat pipe operating at condenser temperatures between 153 and 283 K, Appl. Therm. Eng. 185 (2021) 116349.
[51] Y. Xie, Z. Fang, H. Zhang, et al., Visualization study on operating performance of a dual compensation chamber loop heat pipe under acceleration condition, Appl. Therm. Eng. 217 (2022) 119157.
[52] Y. Xie, W. Pu, S. Liu, et al., Visualized experimental study on steady-state performance of a loop heat pipe under elevated acceleration fields, Appl. Therm. Eng. 238 (2024) 121984.
[53] X. Zhou, L. Hua, B. Shao, et al., Visualization of vapor–liquid interface and optimization in vapor grooves of loop heat pipe, Appl. Therm. Eng. 125724 (2025).
[54] T.A. Edison, J.V. Sengers, Thermodynamic properties of ammonia in the critical region, Int. J. Refrig 22 (5) (1999) 365–378.
[55] H.W. Coleman, W.G. Steele, Experimentation, validation, and uncertainty analysis for engineers, John Wiley & Sons, 2018.
[56] Z.H. Kou, H.T. Lv, W. Zeng, et al., Comparison of different analytical models for heat and mass transfer characteristics of an evaporating meniscus in a micro-channel, Int. Commun. Heat Mass Transfer 63 (2015) 49–53.

[57] Y. Xie, J. Zhang, L. Xie, et al., Experimental investigation on the operating characteristics of a dual compensation chamber loop heat pipe subjected to acceleration field, Appl. Therm. Eng. 81 (2015) 297–312.
[58] Y. Xie, Y. Zhou, D. Wen, et al., Experimental investigation on transient characteristics of a dual compensation chamber loop heat pipe subjected to acceleration forces, Appl. Therm. Eng. 130 (2018) 169–184.
[59] L. Han, Y. Xie, J. Zhu, et al., Experimental and analytical study of dual compensation chamber loop heat pipe under acceleration force assisted condition, Int. J. Heat Mass Transf. 153 (2020) 119615.